Glucose electrooxidation on carbon supported NiAu electrocatalysts

Weliton Silva Fonseca, Thibault C Rafaïdeen, Hamza Kahri, Têko W. Napporn, Christophe Coutanceau

Electrochimica Acta 510 (2025) 145367

Contents lists available at ScienceDirect

Electrochimica Acta

journal homepage: www.journals.elsevier.com/electrochimica-acta

Glucose electrooxidation on carbon supported NiAu electrocatalysts

Weliton Silva Fonseca [a], Thibault Rafaïdeen [a], Hamza Kahri [b], Têko W. Napporn [a,c], Christophe Coutanceau [b,c,*]

[a] CNRS, Université de Poitiers, Institut de Chimie des Milieux et Matériaux de Poitiers-IC2MP, Poitiers, France
[b] Université de Poitiers, CNRS, Institut de Chimie des Milieux et Matériaux de Poitiers-IC2MP, Poitiers, France
[c] French Research Network on Hydrogen (FRH2) of CNRS, France

ARTICLE INFO

Keywords:
Activity
Gluconic acid
Glucose oxidation reaction
Gold
Hydrogen nickel
Selectivity

ABSTRACT

NiAu/C nanomaterials are synthesised using a wet chemistry method with targeted Au atomic ratios of 10 %, 20 % and 30 %. Physicochemical characterisations indicate that the materials have mean compositions close to the nominal ones but ca. 20 at% Au richer in average than expected (Au ratios of 13.6 at%, 23.1 at% and 35.9 at%, respectively). The NiAu/C materials are composed of Au-rich spherical-like Janus particles of several tenths nm and of a phase of very small Ni-rich nanoparticles and $Ni(OH_2)$ clusters. The electrochemical measurements in a 0.1 M NaOH/0.1 M glucose electrolyte indicate that the NiAu20/C catalyst is the most active for the glucose oxidation reaction, leading to a mass activity at +0.6 V vs RHE >1.5 times higher than that with a pure Au/C catalyst, although the Au content is almost 5 times lower. The chronoamperometry measurements for 900 s at +0.6 V vs RHE confirm the activity gain with the NiAu20/C catalyst. The electrolysis measurement at a cell voltage of + 0.6 V for 6 h shows that the NiAu20/C catalyst is selective towards the production of gluconic acid, with a faradaic efficiency higher than 100 %, indicating the occurrence of a 1-electron reaction with anodic hydrogen coproduction. At +0.8 V, the faradaic efficiency is lower than 100 %, indicating the formation of other products than gluconic acid, but at a very low extent (not detectable by HPLC) guarantying a very high selectivity towards gluconic acid.

1. Introduction

To face the challenge of the net-zero emission in 2050, two radical transitions are necessary to move from fossil carbon and energy resources (petroleum, natural gas, coal) toward (i) renewable carbon sources (biomass) and (ii) renewable energy sources (solar photovoltaics, wind turbines, hydropower, etc.), respectively [1]. The massive electrification of the industry and society needed for the energy transition will also involve the partial replacement of thermochemical processes by electrochemical processes for renewable carbon conversion. In this context, the biomass-assisted water electrolysis is a technology that attracts more and more attention [2] because it relies on a non-thermal conversion process and biomass is the most abundant contemporary source of carbon, and therefore the best renewable CO_2-neutral substitute to fossil resources.

As per a report from the S2Biom European Project in 2016, ca. 1 billion tons of biomass could be annually better valorised in Europe [3], and the amount reaches ca. 173 billion tons worldwide [4]. Lignocellulosic biomass is a non-edible waste from forestry and agriculture, composed of cellulose as the largest fraction (40–50 wt%), hemicellulose (20–40 wt%) and lignin (20–30 wt%) [5]. Since cellulose contains only glucose units and hemicellulose is composed of both glucose and xylose units, glucose represents the most abundant biosourced molecule [6]. According to the free energy of glucose electrooxidation into CO_2 (Eq. (1)), the corresponding electrochemical potential under standard conditions at 25 °C is −0.012 V vs SHE (standard hydrogen electrode). This value is significantly lower than that of the standard water oxidation potential (+1.23 V vs SHE) [7].

$$C_6H_{12}O_6 + 6\ H_2O \rightarrow 6\ CO_2 + 24\ H^+ + 24\ e^-\ E^\circ = -0.012\ \text{V vs SHE} \quad (1)$$

On the other hand, the hydrogen evolution reaction (Eq. (2)) is the same for both systems, and the standard potential associated with this reaction is 0.0 V vs SHE.

$$2\ H^+ + 2\ e^- \rightarrow H_2\ E^\circ = 0.000\ \text{V vs SHE} \quad (2)$$

The electrical energy (W_e) consumed for the electrochemical

* Corresponding author.
E-mail address: christophe.coutanceau@univ-poitiers.fr (C. Coutanceau).

https://doi.org/10.1016/j.electacta.2024.145367
Received 1 July 2024; Received in revised form 24 October 2024; Accepted 16 November 2024
Available online 17 November 2024

production of renewable hydrogen from any molecule depending ultimately only on the applied cell voltage U_{cell} (Eq. (3)), i.e. the difference between the anode potential E^+ and the cathode potential E^-, the thermodynamics indicate that glucose electro-reforming should allow saving energy for the production of hydrogen in comparison with water splitting.

$$W_e\left(in\ \text{kWh kg}_{H_2}^{-1}\right) = \frac{zF}{3600 \times M_{H_2}} U_{cell} \quad (3)$$

where z is the number of electrons involved for the production of one molecule of H_2 ($z = 2$), F the Faraday constant ($F = 96{,}485\ C\ mol^{-1}$) and M_{H2} the molar weight of the hydrogen molecules (2×10^{-3} kg mol^{-1}).

For its deployment in biorefineries, this technology must provide huge advantages with respect to the most mature ones [8]. First, the glucose oxidation reaction (GOR) must be much faster than the sluggish oxygen evolution reaction (OER) taking place at the anode of conventional water electrolysers [9], which requires the development of active electrocatalysts. Second, whilst oxygen is not typically recovered in conventional water electrolysis systems, the production of de-fossilised platform molecules at the anode of a biomass-assisted water electrolyser could provide an additional profit [10], which requires the development of selective electrocatalysts. Platinum (Pt) [11,12], palladium (Pd) [13,14] and gold (Au) [15–17] have been extensively studied for the GOR. In addition to being expensive, Pt and Pd are not selective as they are able to break C—C bonds of the glucose molecule from low electrode potentials [18], which also leads to the formation of strongly adsorbed species (CO_{ads}) that poison their surfaces [19,20]. In the case of Au, a good activity for the GOR and a higher selectivity toward gluconic acid than with Pt and Pd are obtained, but Tominaga et al. [21] showed a surface deactivation linked to the formation of a close-packed layer of vertically adsorbed gluconic or xylonic acid molecules.

Alkaline conditions offer higher efficiencies for sugar oxidation reactions and are compatible with efficient PGM-free electrodes. For example, nickel (Ni) is known to be electroactive toward the GOR [22–24] for potentials above ca. +1.2 V vs RHE. It has been proposed that the glucose oxidation reaction was mediated by the Ni(II)/Ni(III) redox transition and involved both an electrochemical and a chemical steps [25,26].

$$Ni(OH)_2 + OH^- \rightarrow NiOOH + H_2O + e^- \text{ electrochemical step} \quad (4)$$

$$NiOOH + C_xH_yO_z \rightarrow Ni(OH)_2 + \text{products chemical step} \quad (5)$$

But the onset potential of glucose oxidation on $Ni(OH)_2$ surface (ca. +1.2 V vs RHE) is generally lower than that observed for the $Ni(OH)_2$/NiOOH transition (ca. +1.3 V vs RHE). Oliveira et al. [27] and Gaith et al. [28] made the same observation for the glycerol electrooxidation reaction and explained that the very early steps of the $Ni(OH)_2$/NiOOH transition were primordial to start the glycerol oxidation reaction. Recent experimental study combined with *in-situ* Fourier transform infrared spectroscopy and high performance liquid chromatography analyses indicated the possibility in the low potential region of a glucose adsorption step on $Ni(OH)_2$ sites via a C–O bond formation between negatively charged Ni−O$^-$ surface species and the carbon atoms of the glucose molecule [29]. Another one combined with microkinetic modelling evidenced a dual-path mechanism at high potential involving an Eley-Rideal and a Langmuir-Hinshelwood pathways with NiOOH reacting with glucose either from the solution or adsorbed on $Ni(OH)_2$ sites [30].

It is known that interactions between different metals can improve the catalytic activity and limit the poisoning effect [19,31] through (i) the bi-functional mechanism [32,33], where the second metal adsorbs (activates) OH species from water or hydroxyl ions to complete the oxidation reaction and desorb the adsorbed organic intermediates, or (ii) the ligand effect [34,35], where a change in the cell parameter affects the electronic density of states close to the Fermi level, and further the adsorption process and adsorption strength of species, which at last will modify the reaction route, intermediates and products. AuNi composites have recently received great interest as glucose sensor owing to their high activity towards glucose oxidation [36,37].

Here we will demonstrate that the modification of carbon-supported nickel nanoparticles by low amounts of Au ($\leq$ 20 at%) could allow achieving higher activity for the GOR, and selectivity and faradaic efficiency toward gluconic acid, than a pure Au/C catalyst. Such achievements could open the possibility of developing a continuous electrochemical reactor allowing the selective production of gluconic acid and hydrogen. To reach these objectives, carbon-supported NiAu nanoparticles (NPs) are first synthesized and characterized, and then their potential for the selective electrooxidation of glucose into gluconic acid, an important bio-based platform molecule belonging to the Top-30 list of value-added chemicals derived from biomass [38,39], determined. Catalysts are synthesized using a green chemistry approach inspired by a procedure described by Dubau et al. [40] for the preparation of hollow PtNi materials deposited on a carbon powder. To maintain a reasonable price of the catalysts, the Au atomic ratio in the reaction mixture for the synthesis of Ni-based catalysts is kept lower than 30 % with respect to Ni. The NiAu/C materials are comprehensively characterized using inductively coupled plasma – optical emission spectroscopy (ICP-OES), scanning and transmission electron microscopy (SEM and TEM), energy dispersive spectroscopy (EDS) mapping, X-ray diffraction (XRD) and X-ray photoelectron spectroscopy (XPS). Then, their electrochemical behaviour, catalytic activity and stability toward the GOR are assessed in alkaline medium in a classical 3-electrode electrochemical cell. At last, the best catalyst in terms of activity is used in the anode of an electrolysis cell to accumulate the reaction products and determine not only the conversion rate and stability of the electro-conversion process, but also the selectivity and faradic efficiency of the system towards the production of gluconic acid.

2. Experimental

The procedure of Dubau et al. [40] for the synthesis of carbon-supported hollow PtNi NPs was adapted for the NiAu/C systems. Typically, 60 mg of carbon powder Vulcan XC72 (Cabot Corp., Inc.) were dispersed in 30 mL ultrapure water (MilliQ®, Millipore, 18.2 MΩ cm, < 2 ppb total organic carbon) and the desired amounts of tetrachloroauric acid ($HAuCl_4{\cdot}3H_2O$, 99.99 % purity, Alfa Aesar) and nickel chloride ($NiCl_2{\cdot}6H_2O$, 99.99 % purity, Sigma Aldrich) were added to reach $100 \times n_{Au}/(n_{Ni}+n_{Au})$ proportions of 0 % (Ni/C), 10 % (NiAu10/C), 20 % (NiAu20)/C, 30 % (NiAu30/C) and 100 % (Au/C), with a target total metal loading of 35 wt% on carbon. A 5 mL aqueous solution of 0.22 mol L^{-1} sodium borohydride ($NaBH_4$, Reagent Plus, 99 % purity, Sigma Aldrich) was then added to the mixture under magnetic stirring. After 1 h stirring at room temperature, the mixture was filtered over a 0.22 μm hydrophilic PVDF membrane filter (Durapore® from Millipore), and the retentate was washed several times with ultrapure water and dried overnight in an oven at 60 °C.

The bulk composition and the metal loading of catalysts were determined by inductively coupled plasma - optical emission spectroscopy (ICP-OES, Agilent 5100), the surface composition by X-ray photoelectron spectroscopy (XPS, Kratos Axis Ultra DLD, Al $K_{\alpha 1}$ source, 150 W, 300 × 700 μm^2 of analysed area), the microstructure by X-ray diffraction (XRD, PANalytical Empyrean X-ray diffractometer), the morphology by scanning electron microscopy – electron dispersion spectroscopy (SEM – EDS, EB FEG JSM-7900F from Jeol, equipped with a field emission gun and an energy dispersive X-ray spectrometer 6/30 from Brücker), and the mean particle size and composition by transmission electron microscopy - electron dispersion spectroscopy (MET STEM 2100 UHR 200 kV Jeol, 0.19 nm resolution).

The electrochemical measurements were performed at 25 °C in a classical three-electrode cell connected to a Voltalab PGZ402 Potentiostat (Radiometer Analytical) interfaced with a computer. The reference

Table 1
Characterization data of the NiAu/C catalysts: actual metal loadings from TGA, Au atomic ratio from ICP-OES analyses and crystallite sizes (L_v) from XRD measurements.

	Au/C	Ni/C	NiAu10/C	NiAu20/C	NiAu30/C
Metal loading (wt%)	36.3	16.9	19.1	27.7	27.4
Au ratio (at%)	100	0	13.6	23.1	35.9
L_v (nm)	20	–	7.8	15.4	15.4

electrode was a reversible hydrogen electrode (RHE, HydroFlex from Gaskatel) placed into a compartment separated from the cell and connected by a Luggin capillary, the counter electrode was a 3 cm^2 geometric surface area glassy carbon plate. The working electrode was prepared by dispensing on a 3 mm diameter glassy carbon disc (0.0706 cm^2 geometric surface area) a 3 µL droplet of a suspension containing 10 mg of as-synthesized catalyst, 50 µL of 5 wt% Nafion suspension in aliphatic alcohols (Sigma Aldrich), 1.450 mL of isopropanol (99.5 % purity, anhydrous, Sigma-Aldrich) and 4 mL of ultrapure water. It corresponded to a catalytic loading of 77.26 $\mu g_{catalyst}$ cm^{-2}. The cyclic voltammetry measurements were performed at 5 mV s^{-1} and the chronoamperometry measurements at a constant anode potential of +0.6 V vs RHE in a N_2-purged 0.1 mol L^{-1} NaOH aqueous solution as support electrolyte and in the presence of 0.1 mol L^{-1}d-glucose when mentioned. All potentials are quoted to the RHE.

The electrolysis measurements were performed at 20 °C in a 25 cm^2 single filter-press type electrolysis cell at the cell voltages of +0.6 V and +0.8 V. The anode containing the NiAu20/C catalyst and the homemade Pt/C cathode were both loaded with 0.5 mg_{metal} cm^{-2}. A simple blotting paper was used as separator between the anodic and cathodic compartments, both fed at a flow rate of 25 mL min^{-1} with a 30 ml solution of 0.1 M glucose in 0.1 M NaOH. Every hour, an aliquot of 600 µL of the anodic solution was sampled and analysed by HPLC (Varian Prostar HPLC equipped with a Transgenomc ICSep ICECOREGEL 107H column for organic acids, aldehydes, alcohols and ketones molecules separation), with a 0.007 mol L^{-1} H_2SO_4 aqueous solution as eluent at a 0.6 mL min^{-1} flow rate, and with a UV detector set at $\lambda = 210$ nm. The complete set-up for the electrolysis measurements and for the HPLC analyses were already fully described elsewhere [6,19,41].

3. Results and discussion

3.1. Physicochemical characterization of the NiAu/C catalysts

The bulk composition and metal loading of the catalysts were determined by ICP-OES. Results are given in Table 1. All the catalysts display lower metal loadings than the targeted value of 35 wt%, lying between 19 and 28 wt% on the carbon support. All the samples present a slightly higher actual atomic Au ratio than the nominal one, surpassing the initially targeted ratio by ca. 20 % in average.

The XRD patterns of Ni/C and Au/C catalysts were recorded to serve as references for the determination of the structure of the NiAu/C

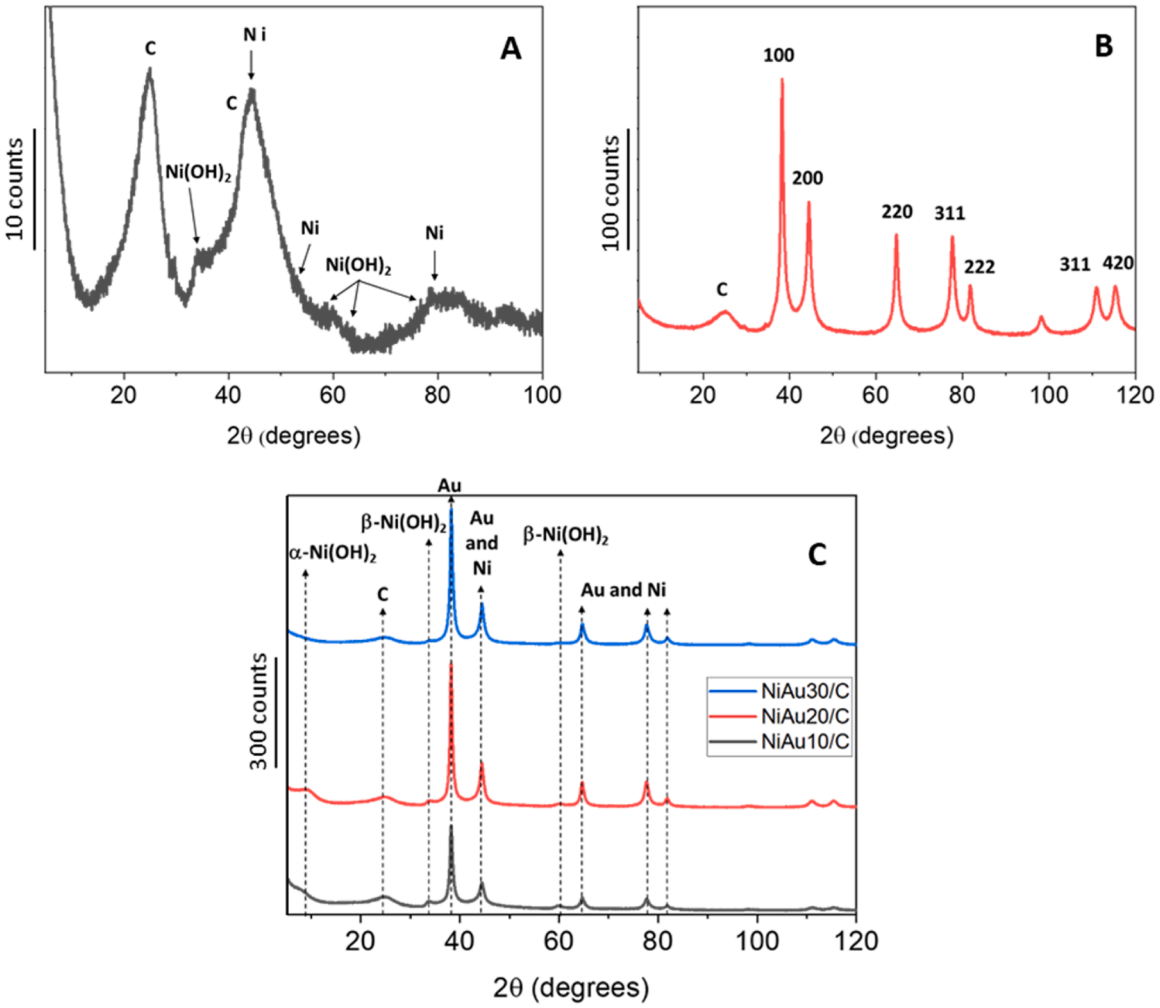

Fig. 1. XRD patterns of the (A) Ni/C, (B) Au/C and (C) NiAu/C catalysts.

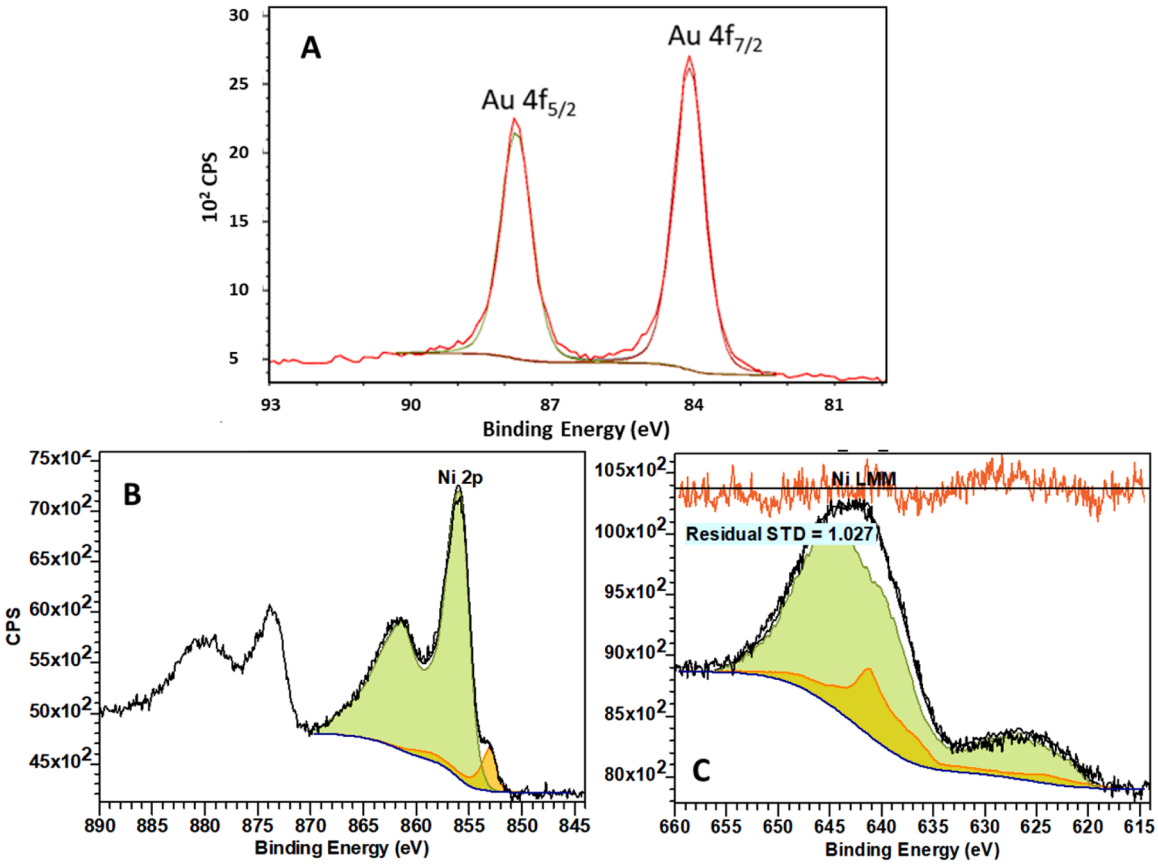

Fig. 2. XPS core level spectra and fit of the spectra recorded on binary NiAu20/C material. (A) in the 80 to 93 eV binding energy region for Au 4f (the red line is the spectra and the brown line the fit), (B) in the 845 to 890 eV binding energy region for Ni 2p (area in orange for Ni^0 and area in green for $Ni(OH)_2$), and (C) in the 615 to 660 eV binding energy region for the Ni LMM (area in orange for Ni^0 and area in green for $Ni(OH)_2$).

catalysts (Fig. 1). Compared to the Au/C material (Fig. 1B), the diffraction peaks recorded on the Ni/C catalyst (Fig. 1A) are broad with a low intensity, which indicates a low crystallinity of the Ni NPs. The diffraction pattern of the Ni/C catalyst exhibits two main broad peaks at 2θ of ca. 25° and 44.4° with a shoulder at ca. 42.9°, and six small peaks at ca. 34.4°, 52.9°, 58.8°, 61.3°, 78.6° and 84° The peak at ca. 25° and the shoulder at ca. 43° are attributed to the {002} and {111} planes of the carbon support, respectively [42,43]. The diffraction peaks at 2θ of ca. 44.4°, 52.9 and 84° can be assigned to the {100}, {200} and {220} planes, respectively, of the face centred cubic (fcc) structure of metallic Ni (JCPDS card no 4–0850). The peaks at 2θ of ca. 34.4°, 58.8°, 61.3° and 78.6° can be indexed as the β-$Ni(OH)_2$ hexagonal phase according to JCPDS card No 14–0117. No peaks corresponding to a Ni-B structure could be evidenced [44]. For the Au/C (Fig. 1B), all the diffraction peaks can be indexed as the fcc phase of metallic Au according to the JCPDS card n° 04–0 784, together with the contributions of the carbon support. The X-ray diffractograms of the NiAu/C catalysts (Fig. 1C) reveal the features of metallic gold fcc structure. Because metallic Ni crystallizes also in a fcc structure an overlay of Au (200) and Ni (111), Au (220) and Ni (200), and Au (222) and Ni (220) diffraction peaks cannot be discarded. It is also possible to observe the presence of small peaks at 2θ of ca. 34.4° and 61.3°, which can be attributed to a β-$(NiOH)_2$ phase, and close to $2\theta = 10°$, which can be assigned to α-$Ni(OH)_2$. The mean size of the gold nanocrystallites was determined from the full width at half maximum of the (100) peak at 2θ of ca. 38.2° (Table 1). The NiAu10/C sample gives the smallest crystallite size (L_v) of ca. 7.8 nm, and the NiAu20/C and NiAu30/C samples presents the same mean crystallite size value of ca. 15.4 nm, whereas pure Au/C has a mean crystallite size of 20 nm.

Due to the higher activity of the NiAu20/C catalyst toward the GOR (see Section 3.2), deeper characterizations were performed on this material. XPS measurements were performed to determine the concentrations and oxidation states of Au and Ni on the catalyst surface (Fig. 2). Two peaks characteristic of Au^0 are observed at 84.07 eV and 87.7 eV (Fig. 2A), which correspond to the binding energies of $Au4f_{7/2}$ and $Au4f_{5/2}$, respectively [45]. For Ni2p (Fig. 2B), $Ni(OH)_2$ and Ni metal have been found to have binding energies of around 856 eV [46] and 852.6 eV [47], respectively. A Ni LMM overlay was carried out to validate the existence of both species, and the match was found to be rather excellent, as shown in Fig. 2C. Based on the fitting, it was discovered that the whole Ni sample contained around 5–7 % of Ni metal. The Au atomic ratio was determined as 21.7 %, only slightly lower than the Au bulk composition of 23.1 % determined by ICP-OES.

TEM coupled with EDS mapping was performed on the NiAu20/C catalyst to evaluate the distribution of the NPs on the carbon support. In Fig. 3A, NPs with diameters from several nm to several tenths' nm are visible. The EDS mapping in Fig. 3B indicates that Au (yellow dot) and Ni (red dot) are homogeneously disseminated over the whole suited area, with the bigger NPs being Au-rich. Fig. 3C shows a typical TEM picture with the determination of the Au atomic ratio in different areas of the sample, which confirms that the very small NPs are Ni-rich, and that bigger NPs are richer in Au.

Furthermore, the EDS results combined with the observed morphology of the particle resembling a hollow sphere (Fig. 3D) support the idea that the NP consists of two distinct faces with different compositions, where one side is predominantly composed of Au while the other side has more Ni sites. The EDS study, in conjunction with the NP's morphology, shed light on the formation of hollow Janus NPs. This observation is consistent with the literature of galvanic replacement of Ni by noble metals; for PtNi, Chattot et al. [48] obtained different PtNi

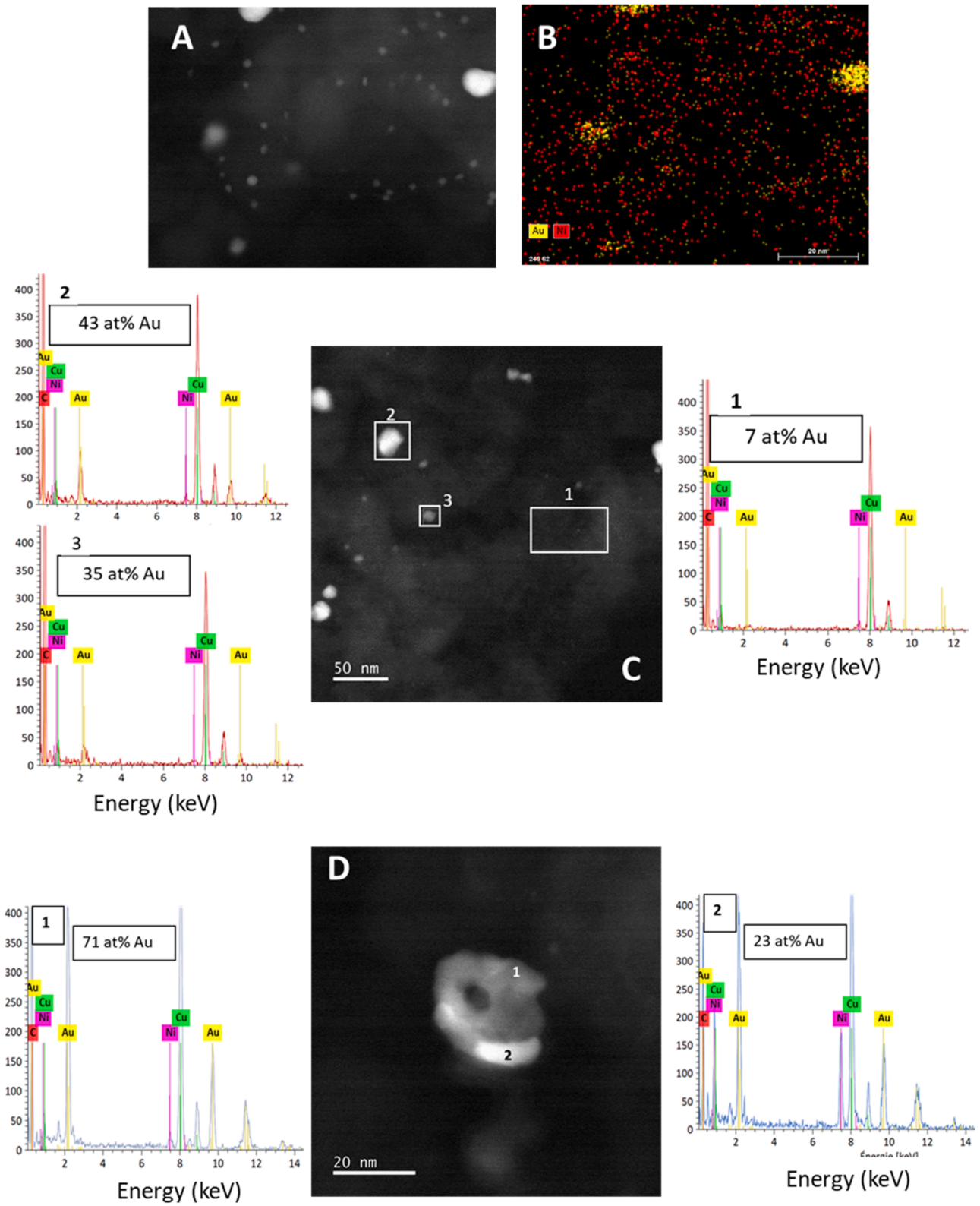

Fig. 3. (A) TEM image of NiAu20/C, (B) EDS mapping of Au (yellow) and Ni (red), (C) TEM image and EDS analysis of different representative areas, and (D) TEM image of a typical Janus particle and EDS analyses in different areas of the particle.

NPs, including as mentioned Janus NPs. Moreover, the segregation into Au-rich and Ni-rich phases is typical of Au-Ni binary systems prepared at temperature below 810 °C: The global composition is proportional to the atomic ratio of the system, but individual NPs will display small inclusions of the lesser element leading to α_1 (Au rich composition with small Ni dopants in the unit cell) and α_2 (Ni rich composition with small Au dopants in the unit cell) structures [49,50]. To summarize, the NiAu20/C catalyst have a mean composition close to the nominal one and seems to be formed of Au-rich spherical-like NPs of several tenths nm (Janus-like and/or hollow NPS), and a phase of very small Ni-rich

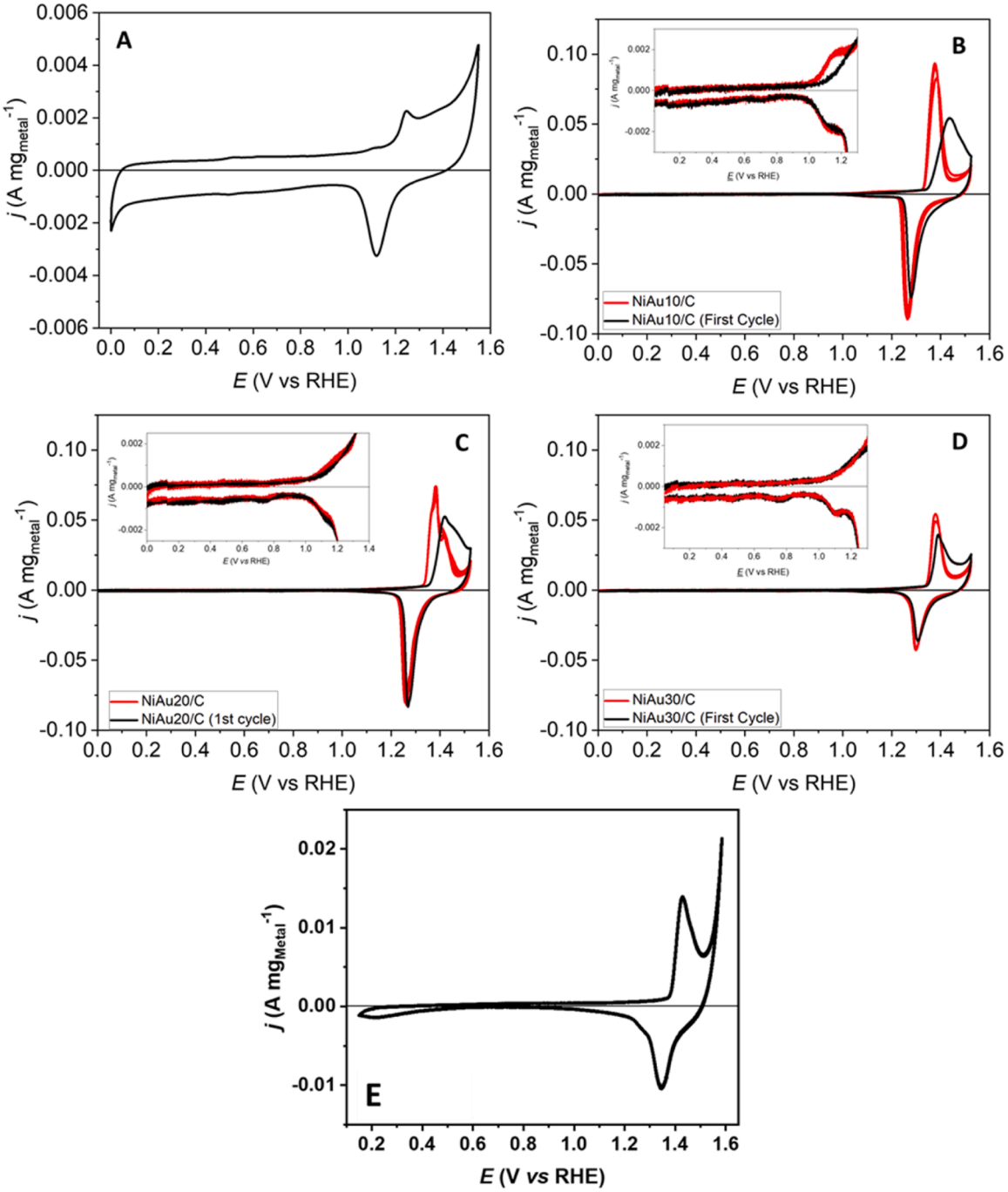

Fig. 4. Cyclic voltammograms of carbon-supported NiAu /C catalysts recorded in N_2-purged 0.1 M NaOH supporting electrolyte (scan rate = 5 mV s^{-1}, T = 25 °C). (A) Au/C, (B) NiAu10/C, (C) NiAu20/C and (D) NiAu30/C and (E) Ni/C. For each graph, an inset present a zoom of the electrochemical features in the potential region from 0 V to +1.3 V vs RHE.

NPs and $Ni(OH_2)$ clusters. It is reasonable to extend this result to the other compositions.

Extrapolating the mechanism proposed by Dubau et al. [40] for the synthesis of PtNi NPs to the present Ni/Au/$NaBH_4$ system, the formation of relatively big Au-rich NiAu particles and Janus-like AuNi NPs could involve first the formation of Ni particles, followed by a reaction of galvanic displacement of Ni^0 atoms by Au^{3+} atoms [51]. The $Au^{III}(Cl)_4^-/Au$ standard redox potential is +1.0 V vs SHE and that of Ni^{2+}/Ni^0 is −0.26 V vs SHE, therefore, the following galvanic displacement reaction can occur [52]:

$$3\ Ni^0 + 2\ Au^{3+} \rightarrow 3\ Ni^{2+} + 2\ Au^0 \quad (6)$$

On the other hand, the formation of $Ni(OH)_2$ clusters can be explained by a mechanism derived from that proposed by Nayak et al. [53] for the synthesis of $Zr(OH)_4$ in a sodium borohydride aqueous solution. This mechanism, also proposed for the synthesis of $Ni(OH)_2$ NPs via a water-in-oil microemulsion method [54], is the following:

$$BH_4^- + 4\ H_2O \rightarrow B(OH)_4^- + 4\ H_2 \quad (7)$$

$$2\ B(OH)_4^- + Ni^{2+} \rightarrow Ni(OH)_2 + 2\ B(OH)_3 \quad (8)$$

And indeed, bubbles (likely hydrogen evolution) were observed when $NaBH_4$ was added to the aqueous solution of metal salts. For the synthesis of NiAu20/C, the pH of the aqueous solution increased from

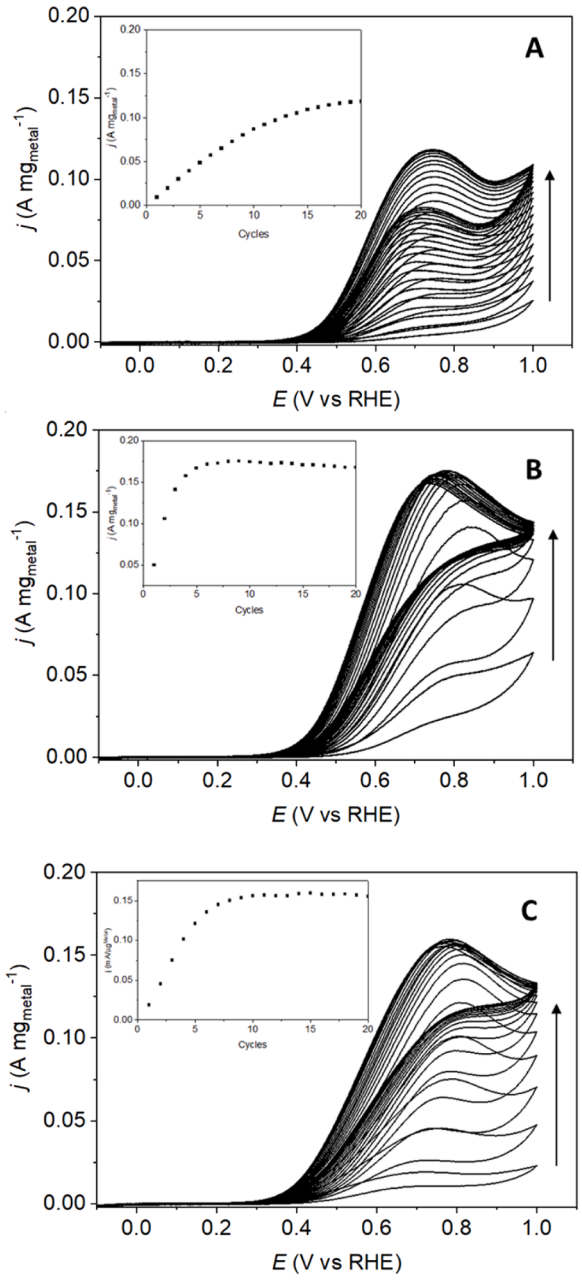

Fig. 5. Polarization curves recorded in a N_2-purged 0.1 M NaOH and 0.1 M glucose electrolyte on (A) NiAu10/C, (B) NiAu20/C and (C) NiAu30/C ($T = 25$ °C, scan rate = 5 mV s^{-1}). For each graph, an inset present the value of the max mass current versus the number of voltammetry cycles.

3.3 before addition of $NaBH_4$ to 8.9 after the reaction, which is a value close to that of the pK_a of the acid boric/borate hydroxide couple (pK_a value of $HB(OH)_4/B(OH)_3$ is 9.2). This pH value enables the formation of $Ni(OH)_2$ species [55]. At last, gold nanoparticles could also be formed through the direct reduction of Au^{3+} ions by $NaBH_4$ [56,57]. All these mechanisms explain the complexity of the structure of the NiAu/C catalysts.

3.2. Electrochemical assessments of the NiAu/C catalysts

The catalysts were electrochemically characterized in a N_2-purged 0.1 M NaOH aqueous electrolyte to probe their surface (Fig. 4). Because the metal loading varied between the different samples, the current was expressed in A mg_{metal}^{-1} with respect to the actual metal mass deposited on the electrode surface (Table 1). The bimetallic catalysts needed an activation process of few tens of voltammetric cycles between +1.0 V and +1.5 V vs RHE to reach a stable voltammograms.

Fig. 4A displays the typical voltammogram of the Au/C catalyst [15] and Fig. 4B to 4D display the voltammograms of the NiAu/C catalysts. For the NiAu/C catalysts, the stable voltammograms obtained after several activation cycles resemble that recorded on a polycrystalline β-$Ni(OH)_2$ material under the same experimental conditions [54]. The redox features related to the $Ni(OH)_2$/NiOOH transitions in the potential region between +1.2 and +1.45 V vs RHE decrease in intensity with the increase of Au content, evidencing the decrease of accessible Ni surface active sites and likely a higher coverage by Au. However, the electrochemical features related to the Au surface oxidation/reduction processes in the +0.8 V to +1.5 V vs RHE potential range can hardly be seen. But insets in Fig. 4B, Fig. 4C and Fig. 4D, for the NiAu10/C, NiAu20/C and NiAu30/C catalysts, respectively, clearly show an oxidation shoulder at ca. +1.2 V vs RHE, and a reduction shoulder at ca. +1.1 V vs RHE, with current densities of the same order as those recorded on the pure Au/C catalysts (Fig. 2A). These features could be assigned to Au surface redox processes in a 0.1 M NaOH aqueous electrolyte [58].

The GOR was studied on the different fresh NiAu/C catalysts. An activation process was needed to reach the highest activity as possible, either in the presence of glucose (Fig. 5) or in the supporting electrolyte alone (Supplementary information, SI 1). After the activation process, stable polarization curves were recorded, with the same feature obtained for each corresponding NiAu/C catalyst independently on the activation methods. It is worth noting that the polarization curves after activation are similar to those recorded on the pure Au/C catalysts [20], indicating that the catalytic activity of the AuNi/C catalysts at low potential (below +1.0 V vs RHE) is driven by the presence of gold active sites. This observation indicates that a surface reconstruction occurs making gold sites more accessible.

It is worth noting that a higher number of activation cycles is needed for the NiAu10/C catalyst to reach a stabilized polarization curve (ca. 15 cycles, inset of Fig. 5A) than for the catalysts with higher Au atomic ratios (between 5 and 10 cycles for the NiAu20/C and NiAu30/C materials, insets of Fig. 5B and 5C, respectively). It is proposed that during the cycling of catalysts with an upper potential limit higher than +1.0 V vs RHE the progressive transition of α-$Ni(OH)_2$ into β-$Ni(OH)_2$ occurs [59]. This progressive transition may decrease the coverage of Au sites by $Ni(OH)_2$ clusters and free active Au surface, as the insertion of water molecules and OH^- species in the interlayers of $Ni(OH)_2$ increases the volume of α-$Ni(OH)_2$ clusters compared to β-$Ni(OH)_2$ clusters [60,61]. Indeed, the SEM images showed an homogeneous dissemination of Ni and $Ni(OH)_2$ clusters on the carbon supports and certainly on the bigger Au-rich nanoparticles.

Fig. 6 compares the stable polarization curves recorded on all the NiAu/C catalysts. The positive scan recorded from 0 V vs RHE to +1.55 V vs RHE on the Au/C material (Fig. 6A) shows an onset potential of ca. +0.3 V vs RHE, a maximum mass current peak at +0.65 V vs RHE, a current plateau from +0.8 V vs RHE to +1.2 V vs RHE and then a decrease of current for higher potentials due to the deactivation of the catalyst by the formation of Au surface oxides [62,63]. The reverse scan (Fig. 6B) displays a huge peaks of surface reactivation at +1.35 V vs RHE [16,64]. The Ni/C catalysts leads also to a classical polarization curve of GOR on $Ni(OH)_2$, with an onset potential close to +1.2 V vs RHE [29, 30].

Considering the activity value of 0.025 A mg_{metal}^{-1} in Fig. 6A, the lower potential of +0.39 V vs RHE is obtained for the positive potential scan with the pure Au/C catalyst and the higher (+0.51 V vs RHE) with the NiAu10/C material; the NiAu20/C leads to a potential of +0.42 V and the NiAu30/C of +0.43 V vs RHE. At a potential of +0.60 V vs RHE, the NiAu20/C catalyst displays the higher activity of 0.19 A mg_{metal}^{-1}, which corresponds to an activity enhancement of 60 % compared with the pure Au/C catalyst (0.12 A mg_{metal}^{-1}). The NiAu10/C catalyst leads to the lower activity (0.056 A mg_{metal}^{-1}), whereas for the NiAu30/C catalyst

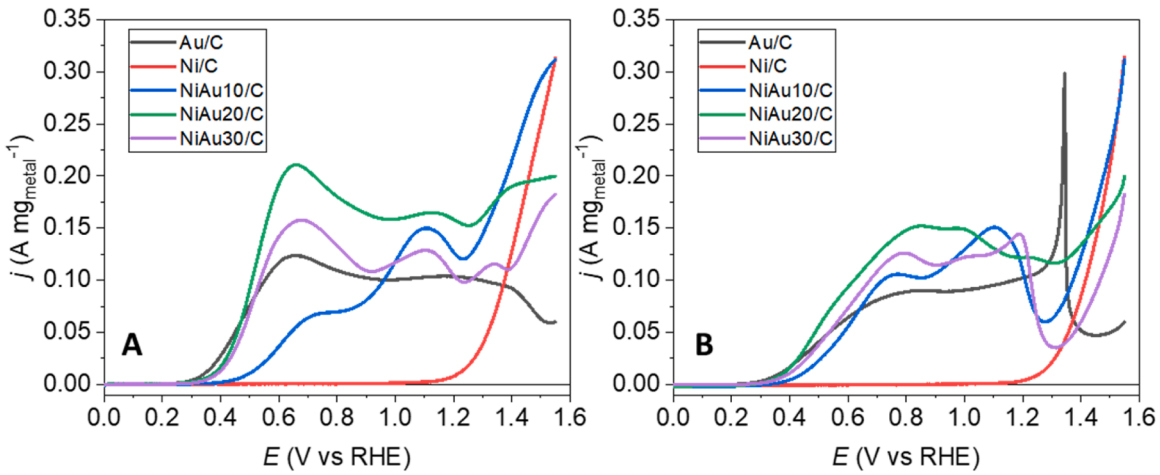

Fig. 6. Polarization curves recorded on the different NiAu/C catalysts for the oxidation of 0.1 M glucose in 0.1 M NaOH. (A) positive scan from 0 V to +1.55 V vs RHE and (B) negative scan from +1.55 V to 0 V vs RHE. (T = 25 °C, scan rate = 5 mV s^{-1}).

Table 2
Electrochemical results for the GOR on the different NiAu/C catalysts.

	E_{onset} (V vs RHE)	E @ 0.025 A g_{metal}^{-1} (V vs RHE)	j @ E = +0.6 V vs RHE (A mg_{metal}^{-1})
Ni/C	+1.10	+1.28	0
NiAu10/C	+0.40	+0.51	0.056
NiAu20/C	+0.30	+0.42	0.19
NiAu30/C	+0.30	+0.43	0.14
Au/C	+0.25	+0.39	0.12

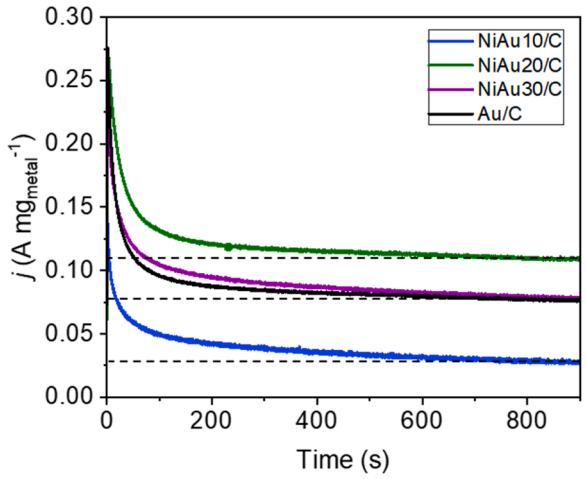

Fig. 7. Chronoamperometry curves recorded at +0.6 V vs RHE for 900 s on the different NiAu/C catalysts for the oxidation of 0.1 M glucose in 0.1 M NaOH. (T = 25 °C).

the activity drops down to 0.14 A mg_{metal}^{-1}. Results are summarized in Table 2, together with the onset potentials (E_{onset}). At a potential of +1.55 V vs RHE, the Ni/C catalyst display the same activity as that of the NiAu10/C materials, indicating the high amount of Ni active sites on this latter catalyst, and the activity decreases with the Au atomic ratio evidencing the decrease of the amounts of accessible Ni sites.

Considering now the reverse scans in Fig. 6B, it is worth noticing that the reactivation peaks at ca. +1.35 V vs RHE observed on Au/C is no more visible for the other catalysts. All these findings point out the existence of a synergetic effect between Au and Ni that makes the NiAu20/C composition the best one for the GOR in terms of activity. This observation is confirmed by chronoamperometry measurements performed at a potential of +0.6 V vs RHE for the GOR (Fig. 7). Following a steep decrease of the activity over the first 200 s, the mass currents stabilize after 900 s at different values according to the catalyst. It is worth noticing that the Au/C catalyst doesn't reach complete surface poisoning as 27.5 % of the initial activity is maintained after 900 s (from 0.28 A mg_{metal}^{-1} initially to 0.076 A mg_{metal}^{-1} after 900 s). Tominaga et al. [21] studied the GOR on an Au plate using electrochemical quartz nanobalance at an electrode potential higher than that of the maximum current peak and observed a steep decrease of the current towards 0 after 10 min; they concluded to a strong poisoning of the Au surface by linearly adsorbed gluconate molecules. Here, we carried out the chronoamperometry measurement at a potential lower than the maximum peak current, likely involving a different mechanism than that at higher potential, which can explain the discrepancy with Tominaga's results. Faverge et al. [18] and Neha et al. [20] proposed indeed different GOR mechanisms on gold nanostructured surfaces according to the potential region: (i) for potentials lower than that of the maximum peak current, an Eley-Rideal type mechanism involving the adsorption of glucose, the formation of intermediates and their hydrolysis into gluconate by OH^- in solution, and (ii) a Langmuir-Hinshelwood type mechanism involving both the adsorption of glucose and OH at the Au surface, and the reaction between both to form gluconate for potentials higher than that of the maximum peak current. The NiAu20/C catalyst achieves the highest stable activity after 900 s with 0.11 A mg_{metal}^{-1}, which corresponds to 40 % of the initial activity (0.27 A mg_{metal}^{-1}) and to an improvement by 45 % of the activity compared with the Au/C catalyst. The higher activity decreases of 80 % was obtained with the NiAu10/C catalyst (from 0.14 A mg_{metal}^{-1} initially to 0.028 A mg_{metal}^{-1} after 900 s). The NiAu20 composition led to better stability and better long terms activity highlighting again, the synergetic effect for this composition, even if its nature is not yet understood.

3.3. Electrolysis measurements

To assess the selectivity of the NiAu20/C catalyst that already showed the highest activity and stability amongst the studied catalysts in this work, electrolysis of a 0.1 M glucose in 0.1 M NaOH solution has been performed at cell voltages of +0.6 V and +0.8 V and the reaction products analysed by HPLC (Supplementary information, SI 2). Because the counter reaction at the cathode is the hydrogen evolution reaction, it has already been shown that for low current densities the cell voltage is imposed by the anode potential, being only a bit lower in reason of the

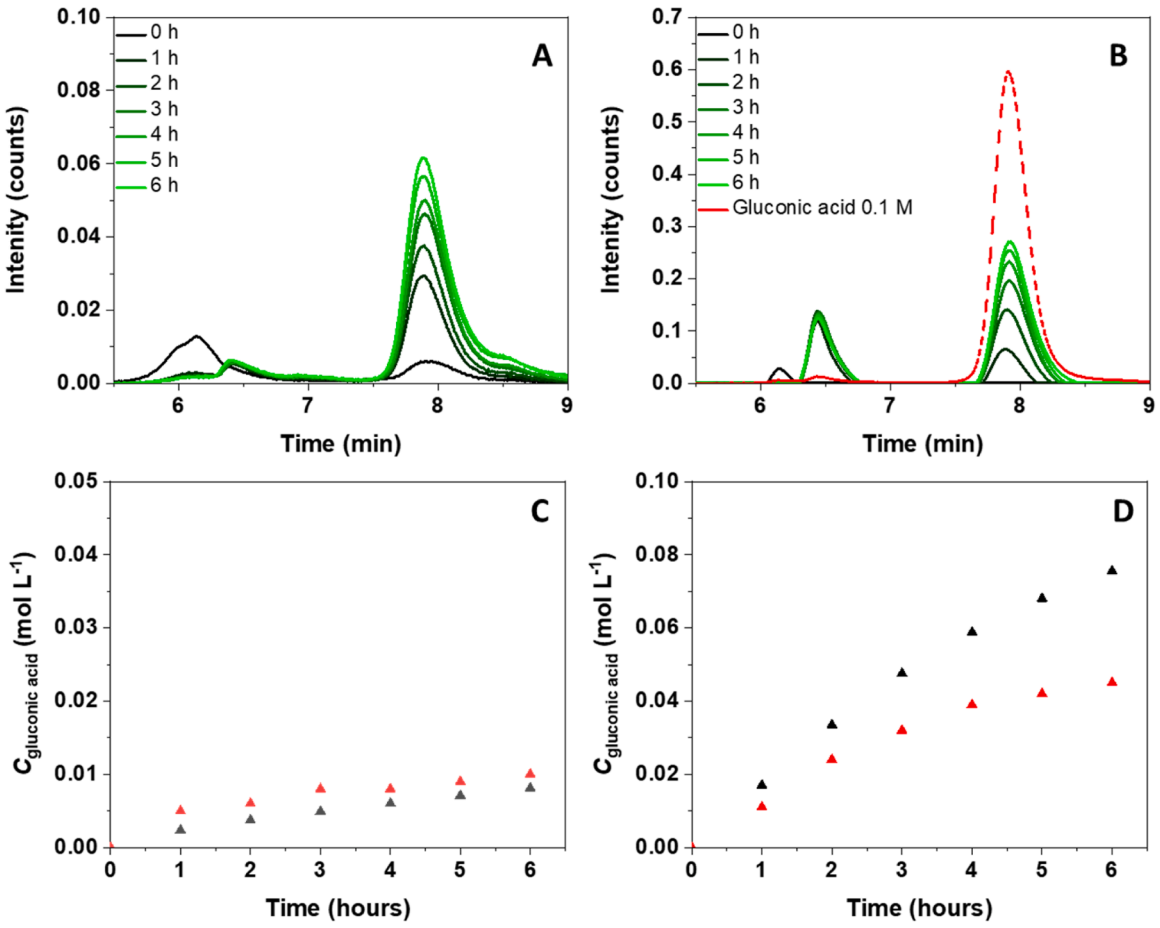

Fig. 8. Chromatograms recorded as a function of time for the 6-hour electrolysis of 0.1 M glucose in 0.1 M NaOH aqueous solution at 20 °C (A) at +0.6 V and (B) at +0.8 V (shade line from black for 0 h to light green for 6 h, the red chromatogram is for a 0.1 M gluconic acid standard solution); Comparison of the theoretical concentrations of gluconic acid determined from charges involved assuming 100 % selectivity and a 2-electron process (black triangles) with the experimental ones determined by HPLC (red triangles) at (C) +0.6 V and (D) +0.8 V.

small HER overpotential [6,19,41].

Fig. 8A and 8B present the chromatograms recorded every hours of electrolysis at +0.6 V and +0.8 V, respectively. Gluconic acid (retention time of 7.9 mn) is by far the main reaction product for both cell voltages, which is expected for glucose oxidation on a gold surface [65]. The peak at a retention time of 6.45 mn is present as soon as the first injection and doesn't increase with time. It is then not related to the formation of a product from electrolysis, but to an impurity or to an experimental artefact. Fig. 8C and 8D compare the actual gluconic acid concentrations determined by HPLC as a function of electrolysis time to the theoretical ones calculated from the integration of the electrical charge and considering two electrons for the oxidation of glucose into gluconate according to the following equation:

$$C_6H_{12}O_6 + 3\ OH^- \rightarrow C_6H_{11}O_7^- + 2\ H_2O + 2\ e^- \quad (9)$$

At a cell voltage of +0.6 V the actual concentration values determined by HPLC are always higher than the theoretical ones from electric charge integration. This means that the number of electrons exchanged is overestimated by the model. Indeed, the faradaic yield is calculated according to Eq. (10) [66].

$$FE = \frac{zFC_{actual}}{Q_{total}} \times 100 \quad (10)$$

where z is the number of electrons to produce one molecule of gluconate, F the Faraday constant (F = 96,485 C mol^{-1}), C_{actual} is the gluconate concentration determined by HPLC and Q_{total} the total electric charge involved for electrolysis.

Table 3
Faradaic efficiency (FE) ta a function of electrolysis time at U_{cell} = 0.6 V and 0.8 V.

	Electrolysis time (h)					
	1	2	3	4	5	6
FE @ +0.6 V (%)	200	160	163	133	128	124
FE @ +0.8 V (%)	65	72	68	66	62	60

If considering z = 2, then FE becomes > 100 % (Table 3). Therefore, z is lower than 2. This finding confirms the proposition of Faverge et al. [18] and Neha et al. [20] for the oxidation of glucose into gluconate following two competitive mechanisms, one through the exchange of one electron and the anodic production of molecular hydrogen and the other through the exchange of two electrons and the anodic production of water. This phenomenon of electrochemical oxidative dehydrogenation (EOD) of aldehydes [67] or sugars [18,20] occurs at low anode potential mainly on Au, Ag and Cu-based materials [68]. This process allows producing hydrogen at both the anode and the cathode according to the following anodic equations:

$$C_6H_{12}O_6 + 2\ Au \rightarrow C_6H_{11}O_6\text{-}Au + Au\text{-}H \quad (10a)$$

$$C_6H_{11}O_6\text{-}Au + 2\ OH\text{-} \rightarrow C_6H_{11}O_7^- + H_2O + 1\ e^- \quad (11)$$

$$Au\text{-}H \rightarrow Au + ½\ H_2 \quad (12)$$

The electron released will serves to the reduction of water at the cathode of the electrolysis cell according to the following cathodic reaction:

$$H_2O + 1\ e^- \rightarrow ½\ H_2 + OH^- \quad (13)$$

Therefore, the production of one mole of hydrogen involves only the transfer of 1 mole of electron instead of 2 in a classical electrolysis cell. Since according to Eq. (2) the electrical energy consumption W_e for the production of hydrogen is only proportional to the number of exchanged electrons and the cell voltage, the electrooxidation of glucose at potentials between +0.3 V and +0.75 V vs RHE, which according to Faverge et al. [18] corresponds to the potential range where anodic H_2 production occurs, will allow decreasing the electrical energy for hydrogen production by a factor greater than 5 (considering a working voltage of +1.8 V for an alkaline electrolysis cell). Now, considering that the NiAu20/C catalyst contains only 23.1 wt% of gold, and that its mass activity at +0.6 V vs RHE is 1.6 higher than that of the Au/C catalysts, it appears that the gain in activity based on Au content for a glucose-assisted water electrolysis is multiplied at least by a factor 7.5.

At a cell voltage of +0.8 V the actual concentration values are always lower than the theoretical ones, which means that the number of electrons exchanged is underestimated by the model and that overoxidized products are formed. However, the overoxidation of one molecule of glucose into low-carbon chain will consume a huge number of electrons. For example, if considering that xylonate is formed from glucose together with carbonate (scission of the C—C bond), according to the following equation:

$$C_6H_{12}O_6 + 9\ OH^- \rightarrow C_5H_9O_6^- + CO_3^{2-} + 6\ H_2O + 6\ e^- \quad (14)$$

then, 6 electrons instead of 2 are consumed, which decreases dramatically the faradaic efficiency (Table 3) but not the selectivity towards gluconate as few other compounds are formed [19]. And indeed, these degradation products are not detected by HPLC, which confirms that they are formed as trace amounts.

4. Conclusion

NiAu/C nanoparticles were successively synthesized by adapting a method developed by Dubau et al. [40] and Chattot et al. [48] for the formation of hollow and Janus PtNi/C nanoparticles. Under the experimental conditions of this work, the gold atomic ratio was varied from 13.6 % to 35.9 %, as determined by ICP-OES and XPS. The electroactivity of catalysts was assessed and the NiAu20/C material led to the highest current densities in the potential range from 0.45 V to 1.3 V vs RHE. The mass activity recorded at +0.6 V vs RHE on NiAu20/C was 1.6 times higher than that on pure Au/C catalyst, although a very low Au ratio of 23.1 at%. Moreover, chronoamperometry measurements at +0.6 V vs RHE showed that after 900 s, the NiAu20/C catalyst maintained 40 % of its initial activity, against only 27.5 % for Au/C. The surprisingly high activity and stability of the Au-based electrodes is proposed to derive from interactions between nickel and gold. Electrolysis in recirculation mode of 0.1 M glucose in 0.1 M NaOH solution at cell voltage of +0.6 V led to the selective production of gluconic acid, but with a faradaic efficiency higher than 100 % considering a 2-electron process. This showed that a 1-electron process with anodic H_2 production occurred simultaneously with the 2-electron process. This phenomenon could lead to a decrease of the electrical energy for hydrogen production by a factor greater than 5 (considering a working voltage of +1.8 V for an alkaline electrolysis cell). Now, considering that the NiAu20/C catalyst contains only 23.1 wt.% of gold, and that its mass activity at +0.6 V vs RHE is >1.5 higher than that of the Au/C catalysts, it appears that the gain in activity based on Au content for a glucose-assisted water electrolysis is multiplied at least by a factor 7.5.

CRediT authorship contribution statement

Weliton Silva Fonseca: Writing – original draft, Methodology, Investigation, Formal analysis. **Thibault Rafaïdeen:** Writing – review & editing, Methodology, Investigation, Formal analysis, Data curation. **Hamza Kahri:** Methodology, Investigation, Formal analysis. **Têko W. Napporn:** Writing – review & editing, Supervision, Formal analysis, Conceptualization. **Christophe Coutanceau:** Writing – review & editing, Validation, Supervision, Funding acquisition, Data curation, Conceptualization.

Declaration of competing interest

The authors declare that they have no known competing financial interests or personal relationships that could have appeared to influence the work reported in this paper.

Acknowledgements

The authors thank the French National Research Agency (ANR) for funding through the Gluconic project (ANR-20-CE43–0005 grant), and the European Union (ERDF), the Région Nouvelle Aquitaine, and the INCREASE research federation (FR CNRS 3707) for supports. This work also pertains to the French government program "Investissements d'Avenir" (EUR INTREE, reference ANR-18-EURE-0010).

Supplementary materials

Supplementary material associated with this article can be found, in the online version, at doi:10.1016/j.electacta.2024.145367.

Data availability

Data will be made available on request.

References

[1] International Energy Agency. Net Zero by 2050: a roadmap for the global energy sector. 4th revision, October 2021. https://iea.blob.core.windows.net/assets/deebef5d-0c34-4539-9d0c-10b13d840027/NetZeroby2050-ARoadmapfortheGlobalEnergySector_CORR.pdf (accessed on March 7th, 2024).
[2] C. Dolle, N. Neha, C. Coutanceau, Electrochemical hydrogen production from biomass, Curr. Opin. Electrochem. 31 (2022) 100841, https://doi.org/10.1016/j.coelec.2021.100841.
[3] C. Panoutsou. Overview report on the current status of biomass for bioenergy, biofuels and biomaterials in Europe (2016).
[4] M. Mujtaba, L. Fernandes Fraceto, M. Fazeli, S. Mukherjee, S.M. Savassa, G. Araujo de Medeiros, A. do Espírito Santo Pereira, S.D. Mancini, J. Lipponen, F. Vilaplana, Lignocellulosic biomass from agricultural waste to the circular economy: a review with focus on biofuels, biocomposites and bioplastics, J. Clean. Prod. 402 (2023) 136815, https://doi.org/10.1016/j.jclepro.2023.136815.
[5] P. McKendry, Energy production from biomass (part 1): overview of biomass, Bioresour. Technol. 83 (2002) 37–46, https://doi.org/10.1016/S0960-8524(01)00118-3.
[6] T. Rafaïdeen, S. Baranton, C. Coutanceau, Electrooxidation of glucose/xylose mixtures on PdAu based nanocatalysts, ChemElectroChem 9 (2022) e202101575, https://doi.org/10.1002/celc.202101575.
[7] C. Lamy, C. Coutanceau, S. Baranton, Production of clean hydrogen by the electrochemical reforming of oxygenated organic compounds, in: B.G. Pollet (Ed.), Hydrogen and Fuel cells Primers, Elsevier, Amsterdam, 2020, pp. 7–20, https://doi.org/10.1016/B978-0-12-821500-5.00002-3.
[8] C. Coutanceau, N. Neha, T. Rafaïdeen, Electrocatalytic transformation of biosourced organic molecules, Curr. Opin. Electrochem. 38 (2023) 101210, https://doi.org/10.1016/j.coelec.2023.101210.
[9] M. Chatenet, B.G. Pollet, D.R. Dekel, F. Dionigi, J. Deseure, P. Millet, R.D. Braatz, M.Z. Bazant, M. Eikerling, I. Staffell, P. Balcombe, Y. Shao-Horn, H. Schäfer, Water electrolysis: from textbook knowledge to the latest scientific strategies and industrial developments, Chem. Soc. Rev. 51 (2022) 4583–4762.
[10] L. Du, Y. Shao, J. Sun, G. Yin, C. Du, Y. Wang, Electrocatalytic valorisation of biomass derived chemicals, Catal. Sci. Technol. 8 (2018) 3216–3232, https://doi.org/10.1039/C8CY00533H.
[11] H.-W. Lei, B. Wu, C.-S. Cha, H. Kita, Electro-oxidation of glucose on platinum in alkaline solution and selective oxidation in the presence of additives, J. Electroanal. Chem. 382 (1995) 103–110.

[12] A. Brouzgou, P. Tsiakaras, Electrocatalysts for glucose electrooxidation reaction: a review, Top. Catal. 58 (2015) 1311–1327, https://doi.org/10.1007/s11244-015-0499-1.
[13] C.C. Hu, T.C. Wen, Voltammetric investigation of palladium oxides-II. Their formation/reduction behaviour during glucose oxidation in NaOH, Electrochim. Acta 39 (1994) 2763–2771.
[14] S. Song, K. Wang, L. Yana, A. Brouzgou, Y. Zhang, Y. Wang, P. Tsiakaras, Ceria promoted Pd/C catalysts for glucose electrooxidation in alkaline media, Environmental 176 (2015) 233–239.
[15] M. Pasta, F. La Mantia, Y. Cui, Mechanism of glucose electrochemical oxidation on gold surface, Electrochim. Acta 55 (2010) 5561–5568, https://doi.org/10.1016/j.electacta.2010.04.069.
[16] G. Moggia, T. Kenis, N. Daems, T. Breugelmans, Electrochemical oxidation of D-glucose in alkaline medium: impact of oxidation potential and chemical side reactions on the selectivity to D-gluconic and D-glucaric acid, ChemElectroChem 7 (2020) 86–95, https://doi.org/10.1002/celc.201901592.
[17] N. Schlegel, G.K. Wiberg, M. Arenz, On the electrooxidation of glucose on gold: towards an electrochemical glucaric acid production as value-added chemical, Electrochim. Acta 410 (2022) 140023, https://doi.org/10.1016/j.electacta.2022.140023.
[18] T. Faverge, B. Gilles, A. Bonnefont, F. Maillard, C. Coutanceau, M. Chatenet, In situ investigation of D-glucose oxidation into value-added products on Au, Pt and Pd under alkaline conditions: a comparative study, ACS Catal 13 (2023) 2657–2669, https://doi.org/10.1021/acscatal.2c05871.
[19] T. Rafaïdeen, S. Baranton, C. Coutanceau, Highly efficient and selective electrooxidation of glucose and xylose in alkaline medium at carbon supported alloyed PdAu nanocatalysts, Environmental 243 (2019) 641–656, https://doi.org/10.1016/j.apcatb.2018.11.006.
[20] N. Neha, T. Rafaïdeen, T. Faverge, F. Maillard, M. Chatenet, C. Coutanceau, Revisited mechanisms for glucose electrooxidation at platinum and gold nanoparticles, Electrocatalysis 14 (2023) 121–130.
[21] M. Tominaga, M. Nagashima, K. Nishiyama, I. Taniguchi, Surface poisoning during electrocatalytic monosaccharide oxidation reactions at gold electrodes in alkaline medium, Electrochem. Commun. 9 (2007) 1892–1898, https://doi.org/10.1016/j.elecom.2007.04.024.
[22] A. Cardoso de Sá1, L. Lataro Paim, N.Ramos Stradiotto, Int. J. Electrochem. Sci. 9 (2014) 7746–7762.
[23] A.S. Danial, M.M. Saleh, S.A. Salih, M.I. Awad, On the synthesis of nickel oxide nanoparticles by solegel technique and its electrocatalytic oxidation of glucose, J. Power Sources 293 (2015) 101–108.
[24] C. Lin, H. Li, P. Zhang, C. Deng, L. Meng, Q. Zhou, S. Wang, J. Wu, C. Liu, J. Tian, Y. Qian, Boosting water electrolysis with anodic glucose oxidation reaction over engineered cobalt nickel hydroxide nanosheet on carbon cloth, J. Electroanal. Chem. 861 (2020) 113946, https://doi.org/10.1016/j.jelechem.2020.113946.
[25] M. Fleischmann, K. Korinek, D. Pletcher, The oxidation of organic compounds at a nickel anode in alkaline solution, J. Electroanal. Chem. 31 (1971) 39–49, https://doi.org/10.1016/S0022-0728(71)80040-2.
[26] R.M.A. Tehrani, S.Ab Ghani, Electrocatalysis of free glycerol at a nanonickel modified graphite electrode and its determination in biodiesel, Electrochim. Acta 70 (2012) 153–157.
[27] V.L. Oliveira, C. Morais, K. Servat, T.W. Napporn, G. Tremiliosi-Filho, K.B. Kokoh, Studies of the reaction products resulted from glycerol electrooxidation on Ni-based materials in alkaline medium, Electrochim. Acta 117 (2014) 255–262.
[28] M.E. Ghaith, M.G. Abd El-Moghny, H.H. Alalawy, M.E. El-Shakre, M.S. El-Deab, Enhancing the performance of Ni nanoparticle modified carbon felt towards glycerol electrooxidation: impact of organic additive, RSC Adv 13 (2023) 10893–10902, https://doi.org/10.1039/D3RA01197F.
[29] A. Medrano-Banda, E. Ginoux, T. Faverge, A. Oshchepkov, A. Bonnefont, M. Chatenet, C. Coutanceau, G. Kéranguéven, P. Cognet, E. Savinova, Electrochemical oxidation of glucose in alkaline environment - A comparative study of Ni and Au electrodes, Electrochim. Acta 487 (2024) 144159.
[30] A. Medrano-Banda, J. Guehl, G. Kéranguéven, A. Oshchepkov, E. Savinova, A. Bonnefont, Dual-path glucose electrooxidation reaction on $Ni(OH)_2$/NiOOH catalysts in alkaline media, Electrochim. Acta 476 (2024) 143692, https://doi.org/10.1016/j.electacta.2023.143692.
[31] L. Yan, A. Brouzgou, Y. Meng, M. Xiao, P. Tsiakaras, S. Song, Efficient and poison-tolerant PdxAuy/C binary electrocatalysts for glucose electrooxidation in alkaline medium, Appl. Catal. B: Environmental 150–151 (2014) 268–274, https://doi.org/10.1016/j.apcatb.2013.12.026.
[32] M. Watanabe, S. Motoo, Electrocatalysis by ad-atoms: part II. Enhancement of the oxidation of methanol on platinum by ruthenium ad-atoms, J. Electroanal. Chem. Interf. Electrochem. 60 (1975) 267–273.
[33] Y.Y. Tong, S.K. Hee, P.K. Babu, P. Waszczuk, A. Wieckowski, E. Oldfield, An NMR investigation of CO tolerance in a Pt/Ru fuel cell catalyst, J. Am. Chem. Soc. 124 (2002) 468–473, https://doi.org/10.1021/ja011729q.
[34] T. Iwasita, F.C. Nart, W. Vielstich, An FTIR study of the catalytic activity of a 85:15 Pt:ru alloy for methanol oxidation, Ber. Bunsengse. Phys. Chem. 94 (1990) 1030–1034, https://doi.org/10.1002/bbpc.19900940930.
[35] T. Frelink, W. Visscher, J.A.R. Van Veen, Measurement of the Ru surface content of electrocodeposited PtRu electrodes with the electrochemical quartz crystal microbalance: implications for methanol and CO electrooxidation, Langmuir 12 (1996) 3702–370824, https://doi.org/10.1021/la9502709.
[36] L. Wang, W. Zhu, W. Lu, L. Shi, R. Wang, R. Pang, Y.Y. Cao, F. Wan, X. Xu, One-step electrodeposition of AuNi nanodendrite arrays as photoelectrochemical biosensors for glucose and hydrogen peroxide detection, Biosensors Bioelec 142 (2019) 111577, https://doi.org/10.1016/j.bios.2019.111577.
[37] K. Arikan, H. Burhan, E. Sahin, F. Sen, A sensitive, fast, selective, and reusable enzyme-free glucose sensor based on monodisperse AuNi alloy nanoparticles on activated carbon support, Chemosphere 291 (2022) 132718.
[38] T. Werpy, G. Petersen, A. Aden, J. Bozell, J. Holladay, J. White, A. Manheim, D. Elliot, L. Lasure, S. Jones, M. Gerber, K. Ibsen, L. Lumberg, S. Kelley, Pacific northwest national laboratory, national renewable energy laboratory. top value added chemicals from biomass: results of screening for potential candidates from sugars and synthesis gas, Department of Energy, Oak Ridge, TN, 2004. https://www.nrel.gov/docs/fy04osti/35523.pdf (accessed on March 13, 2024).
[39] R. Taylor, L. Nattrass, G. Alberts, P. Robson, C. Chudziak, A. Bauen (E4Tech), I. Marsili Libelli, G. Lotti, M. Prussi, R. Nistri, D. Chiaramonti (RE-CORD), A. López Contreras, H. Bos, G. Eggink, J. Springer, R. Bakker, R. van Ree (tWUR). From the sugar platform to biofuels and biochemicals, final report for the european commission directorate-general energy N° ENER/C2/423-2012/SI2.673791, April 2015.
[40] L. Dubau, T. Asset, R. Chattot, C. Bonnaud, V. Vanpeene, J. Nelayah, F. Maillard, Tuning the performance and the stability of porous hollow PtNi/C nanostructures for the oxygen reduction reaction, ACS Catal 5 (2015) 5333–5534, https://doi.org/10.1021/acscatal.5b01248.
[41] N. Neha, S.R.B. Kouamé, T. Rafaïdeen, S. Baranton, C. Coutanceau, Remarkably efficient carbon-supported nanostructured platinum-bismuth catalysts for the selective electrooxidation of glucose and methyl-glucoside, Electrocatalysis 12 (2021) 1–14, https://doi.org/10.1007/s12678-020-00586-y.
[42] H. Zhu, X. Li, F. Han, Z. Dong, G. Yuan, G. Ma, A. Westwood, K. He, The effect of pitch-based carbon fiber microstructure and composition on the formation and growth of SiC whiskers via reaction of such fibers with silicon sources, Carbon N Y 99 (2016) 174–185, https://doi.org/10.1016/j.carbon.2015.12.002.
[43] H. Yi, H. Wang, Y. Jing, T. Peng, Y. Wang, J. Guo, Q. He, Z. Guo, X. Wang, Advanced asymmetric supercapacitors based on CNT@$Ni(OH)_2$ core-shell composites and 3D graphene networks, J. Mater. Chem. A 3 (2015) 19545–19555, https://doi.org/10.1039/C5TA06174A.
[44] Y. Cheng, M. Tanaka, T. Watanabe, S.Y. Choi, M.S. Shin, K.H. Lee, Synthesis of Ni_2B nanoparticles by RF thermal plasma for fuel cell catalyst, Confer. Ser. 518 (2014) 012026, https://doi.org/10.1088/1742-6596/518/1/012026.
[45] J. Hao, H. Zhu, Y. Li, P. Liu, S. Lu, F. Duan, W. Dong, Y. Lu, T. Liu, M. Du, Tuning the electronic structure of AuNi homogeneous solid-solution alloy with positively charged Ni center for highly selective electrochemical CO_2 reduction, Chem. Eng. J. 404 (2021) 126523, https://doi.org/10.1016/j.cej.2020.126523.
[46] X. Yi, V. Celorrio, H. Zhang, N. Robertson, C. Kirk, a/b-Ni(OH)2 phase control by F-ion incorporation to optimise hybrid supercapacitors performance, J. Mater. Chem. A 11 (2023) 22275–22287, https://doi.org/10.1039/D3TA04731H.
[47] A.P. Grosvenor, M.C. Biesinger, R. St. C. Smart, N.S. McIntyre, New interpretation of XPS spectra of nickel metal and oxides, Surf. Sci. 600 (2006) 1771–1779, https://doi.org/10.1016/j.susc.2006.01.041.
[48] R. Chattot, T. Asset, J. Drnec, P. Bordet, J. Nelayah, L. Dubau, F. Maillard, Atomic-scale snapshots of the formation and growth of hollow PtNi/C nanocatalysts, Nano Lett. 17 (2017) 2447–2453.
[49] T. Yang, C.M. Rodrigues de Almeida, D. Ramasamy, F.J. Almeida Loureiro, A detailed study of Au-Ni bimetal synthesized by the phase separation mechanism for the cathode of low-temperature solid oxide fuel cells, J. Power Sources 269 (2014) 46–53, https://doi.org/10.1016/j.jpowsour.2014.06.151.
[50] C.C. Walker, J. Carothers, M. Roulier, B. Rowell, Brandon. an examination of the Au-Ni phase diagram for magneto-plasmonic applications. (2018). Chancellor's Honors Program Projects.
[51] Y. Umeya, Y. Kobayashi, T. Kawashimo, S. Ahn, G. Chang, M. Oyama, Preparation of gold modified nickel wire electrodes for electroanalysis via a galvanic replacement reaction, Electroanal 30 (2018) 1370–1377, https://doi.org/10.1002/elan.201800077.
[52] J. Reboul, Z.Y. Li, J. Yuan, K. Nakatsuka, M. Saito, K. Mori, H. Yamashita, Y. Xia, C. Louis, Synthesis of small Ni-core–Au-shell catalytic nanoparticles on TiO_2 by galvanic replacement reaction, Nanoscale Adv 13 (2021) 823–835, https://doi.org/10.1039/D0NA00617C.
[53] N.B. Nayak, B.B. Nayak, Aqueous sodium borohydride induced thermally stable porous zirconium oxide for quick removal of lead ions, Scient. Rep 6 (2016) 23175, https://doi.org/10.1038/SREP23175.
[54] S. Tahmasebi, S. Jahangiri, N. Mosey, G. Jerkiewicz, A. Mark, S. Cheng, G. Botton, S. Baranton, C. Coutanceau, Remarkably stable nickel hydroxide nanoparticles for miniaturized electrochemical energy storage, ACS Appl. Energy Mater. 3 (2020) 7294–7305, https://doi.org/10.1021/acsaem.0c00483.
[55] L.-F. Huang, M.J. Hutchison, R.J. Santucci Jr., J.R. Scully, J.M. Rondinelli, Improved electrochemical phase diagrams from theory and experiment: the Ni−water system and its complex compounds, J. Phys. Chem. C 121 (2017) 9782–9789, https://doi.org/10.1021/acs.jpcc.7b02771.
[56] S. Lankiang, M. Chiwata, S. Baranton, H. Uchida, C. Coutanceau, Oxygen reduction reaction at binary and ternary nanocatalysts based on Pt, Pd and Au, Electrochim. Acta. 182 (2015) 131–142.
[57] C. Deraedt, L. Salmon, S. Gatard, R. Ciganda, R. Hernandez, J. Ruiza, D. Astruc, Sodium borohydride stabilizes very active gold nanoparticle catalysts, Chem. Commun. 50 (2014) 14194–14196, https://doi.org/10.1039/c4cc05946h.
[58] K.N. da Silva, S.T. Maruyama, E. Sitta, High order cyclic voltammograms during electrooxidation of ethanol catalyzed by gold, J. Braz. Chem. Soc. Vol. 00 (2017) 1–7, https://doi.org/10.21577/0103-5053.20170020.
[59] A.G. Oshchepkov, G. Braesch, S. Ould-Amara, G. Rostamikia, G. Maranzana, A. Bonnefont, V. Papaefthimiou, M.J. Janik, M. Chatenet, E.R. Savinova, Nickel metal nanoparticles as anode electrocatalysts for highly efficient direct

borohydride fuel cells, ACS Catal. 9 (2019) 8520–8528, https://doi.org/10.1021/acscatal.9b01616.
[60] D.S. Hall, D.J. Lockwood, C. Bock, B.R. MacDougall, Nickel hydroxides and related materials: a review of their structures, synthesis and properties, Proc. R. Soc. A 471 (2014) 0792, https://doi.org/10.1098/rspa.2014.0792.
[61] S. Fujita, S. Baranton, C. Coutanceau, G. Jerkiewicz, Design, synthesis, and characterization of carbon-supported β-ni(oh)$_2$ nanosheets for miniaturized nickel–metal hydride batteries, Energy Technol (2024) 2301268, https://doi.org/10.1002/ente.202301268.
[62] C. Xiang, Q. Xie, S. Yao, Electrochemical quartz crystal impedance study of glucose oxidation on a nickel hydroxide modified au electrode in alkaline solution, Electroanal 15 (2003) 987–990, https://doi.org/10.1002/elan.200390120.
[63] M. Pasta, R. Ruffo, E. Falletta, C.M. Mari, C.Della Pina, Alkaline glucose oxidation on nanostructured gold electrodes, Gold Bull 43 (2010) 57–64.
[64] L.A. Larew, D.C. Johnson, Concentration dependence of the mechanism of glucose oxidation at gold electrodes in alkaline media, J. Electroanal. Chem. Interfacial Electrochem. 262 (1989) 167–182, https://doi.org/10.1016/0022-0728(89)80020-8.
[65] Y. Holade, K. Servat, T.W. Napporn, C. Morais, J.-M. Berjeaud, K.B. Kokoh, Highly selective oxidation of carbohydrates in an efficient electrochemical energy converter: cogenerating organic electrosynthesis, ChemSusChem 9 (2016) 252–263, https://doi.org/10.1002/cssc.201501593.
[66] E. Ginoux, T. Rafaïdeen, P. Cognet, L. Latapie, C. Coutanceau, Selective glucose electro-oxidation catalyzed by TEMPO on graphite felt, Front. Chem. 12 (2024) 1393860, https://doi.org/10.3389/fchem.2024.1393860.
[67] H. Liu, N. Agrawal, A. Ganguly, Y. Chen, J. Lee, J. Yu, W. Huang, M.M. Wright, M. J. Janik, W. Li, Ultra-low voltage bipolar hydrogen production from biomass-derived aldehydes and water in membrane-less electrolyzers, Energy Environ. Sci. 15 (2022) 4175, https://doi.org/10.1039/d2ee01427k.
[68] N.C. Ramos, A. Holewinski, Recent advances in anodic hydrogen production: electrochemical oxidative dehydrogenation of aldehydes to carboxylates, Curr. Opin. Electrochem. (2024), https://doi.org/10.1016/j.coelec.2024.101484.